Optics & Laser Technology 192 (2025) 113602

Contents lists available at ScienceDirect

Optics and Laser Technology

journal homepage: www.elsevier.com/locate/optlastec

Full length article

Coupled surface plasmons and resonant optical tunnelling in symmetric optical microcavities

Alejandro Doval, Yago Arosa, Raúl de la Fuente *

Instituto de materiais da USC - iMATUS, Grupo de Nanomateriais, Fotónica e Materia Branda, Universidade de Santiago de Compostela E-15782 Santiago de Compostela, Spain

ARTICLE INFO

Keywords:
Coupled surface plasmons
Resonance
Microcavity
Evanescent wave
Attenuated optical tunnelling

ABSTRACT

This study presents an analytical model for light transmission through a symmetric optical microcavity. The structure comprises two metallic films separated by a thin layer of a low refractive index dielectric, and embedded within a semi-infinite dielectric of higher refractive index. This configuration supports both volume and surface resonances. The surface resonances result from synchronised collective electronic oscillations at the inner surfaces of the two thin metallic films, called coupled surface plasmons. For clarity, surface resonances are first defined and analysed considering the Drude model for ideal, lossless metal films. The model is then extended using the generalised complex Drude model, which accounts for losses. The results depict that high transmittance is possible even when the thickness of the inner dielectric layer spans several wavelengths. This phenomenon is an enhanced form of frustrated total reflection between dielectrics analogous to the quantum tunnelling effect. The phenomenon is more pronounced because of the two absorbing metal films. Under resonant conditions, these films enable unusually high transmission despite their inherent losses. Experimental results are presented in excellent agreement with the theoretical predictions. This proposed transmission model in a plasmonic microcavity provides a foundation for future theoretical research and potential applications of plasmonic microcavity devices.

1. Introduction

The confinement of light at the interface of a metal and a dielectric material is a well-established phenomenon that has been studied since the latter half of the 20th century [1,2]. When two materials in contact have real parts of their dielectric constants with opposite signs, the interaction of light with the free charges in the medium having a negative dielectric constant can lead to collective electronic oscillation provided a specific synchronism condition is satisfied. This occurs, for example, when a noble metal is in contact with a dielectric material in the visible range. Such metals exhibit a predominantly real and negative dielectric constant, and their conduction electrons are free to couple with incident electromagnetic radiation. These oscillations are known as surface plasmon resonance (SPR). Suppose a very thin metallic or dielectric film is instead sandwiched between two semi-infinite dielectric or metallic materials (resulting in a DMD or MDM structure, respectively). In that case, it becomes possible to induce collective and synchronised oscillations involving both thin-film interfaces. These are called coupled surface plasmons (CSPs) [3].

Initial studies in this field focused on guided resonances or simple plasmonic modes—either at a single surface or within a metallic or dielectric film. The main objective was to establish the resonance conditions and corresponding dispersion curves [4–6]. The ability to observe plasmon resonances via prism coupling encouraged these investigations and facilitated early applications [7]. The two classical configurations of SPR are the Kretschmann and Otto setups. Kretschmann configuration [8] consists of a high-index prism (H), coated with a thin metallic layer (M), on one of its faces, which is then exposed to air or some other low-index dielectric material (L), forming an HML structure. Otto configuration [9], in contrast, consists of a high-index prism (H), in direct contact with a low-index dielectric film (L), which, in turn, is in contact with a thick metal (M), forming an HLM structure. In both cases, the surface plasmon is generated at the ML interface and manifests as a dip in the reflection output of the system because of attenuated total reflection (ATR).

From a strictly physical standpoint, neither the Kretschmann nor the Otto configuration involves guided resonances (modes) at the interface, but rather radiative resonances associated with the HML or HLM

* Corresponding autor at: University of Santiago de Compostela, Department of Applied Physics, Santiago de Compostela, Spain.
E-mail address: raul.delafuente@usc.es (R. de la Fuente).

https://doi.org/10.1016/j.optlastec.2025.113602
Received 7 May 2025; Received in revised form 24 June 2025; Accepted 15 July 2025
Available online 24 July 2025

structures, respectively. This is because the related dip in reflectance corresponds to absorbed rather than guided radiation. Furthermore, although close, the reflection and SPR resonances do not occur at the same incidence angle or wavelength [10]. CSP-related radiative resonances can be observed using a planar microcavity formed by two thin metallic films acting as mirrors, with a low-index intracavity medium between them and surrounded by a high-index dielectric material, that is, an HMLMH structure with possible CSPs localised at the two ML interfaces. These plasmon resonances in microcavities were observed through both reflection [11] and transmission [3,12] measurements, and consequent numerical studies were performed. Although CSP resonances have been applied in various contexts, fundamental theoretical studies remain limited and most of the recent research has focused on practical applications. These include the design of optical filters [13–15] based on transmission resonances, or improving coupling efficiency in the Kretschmann configuration [16–19] based on reflection resonances. In addition, there are several other applications of the structure, such as electroluminescence [20], SPR spectroscopy [21], potential hyperlenses [22,23], thin air gap measurements [24,25], or biosensing [26]. Despite its interest, the mathematical foundation of these applications was not studied, and they were analysed using numerical methods.

The present study revisits the CSP resonances in optical microcavities from a fundamental and analytical perspective. A theoretical model is developed for transmission through a plane metallic cavity, operating in the plasmonic regime (for incidence angles above the critical incidence for an HL interface). The analysis builds on the theory of multiple-beam interference [27], extended here to the plasmonic regime, where the wave within the cavity is evanescent. In this case, the cavity thickness must be in the order of microns, such that total internal reflection (TIR) does not occur at the first mirror, as the corresponding evanescent tail reaches the second mirror. The metallic film must also be thin—no more than a few tens of nanometres—such that light is not completely attenuated when crossing through it. The proposed model establishes a well-defined resonance condition for transmittance maxima for lossless and lossy metals and determines the maximum transmittance value for different cavity thicknesses. A crucial factor in the analysis is the behavior of the mirror amplitude coefficient r_{lmh}, which plays a defining role in the resonance formation within the HMLMH structure.

The manuscript is organised as follows. Section 2 defines the microcavity arrangement and presents the expression of its transmittance as a function of wavelength, angle of incidence, thickness of the central layer, and mirror amplitude coefficients. A sample experimental transmittance map is analysed to check our theoretical predictions. Section 3 addresses transmittance beyond the critical angle for lossless metals, and the resonance condition for unitary transmittance is determined and analysed. The coalescence parameters (θ_{co}, d_{co}) for the two surface resonances are also defined in this part. Section 4 extends these results to the case of lossy metals and includes a detailed analysis of the key role played by the mirror reflection coefficient r_{lmh}. The analysis in these two sections was performed at a constant wavelength with varying incidence angles. Section 5 examines the spectral resonance curve for fixed incidence angles. Section 6 details the experimental set-up and subsequent results, which are in complete agreement with the theoretical analysis results. Finally, the conclusions of this work are presented in Section 7.

2. Transmission through an HMLMH structure

The proposed device comprises a set of five media separated by plane-parallel interfaces. In this symmetric arrangement (Fig. 1) the three central layers form a microcavity. The structure consists of a surrounding dielectric with refractive index n_h (h stands for high), two thin metallic mirrors (which will be referred to using subscript m), and an inner dielectric with refractive index $n_l < n_h$ (l stands for low). The inner dielectric fills the space between the mirrors, which are separated by a distance d, referred to as the "intracavity thickness".

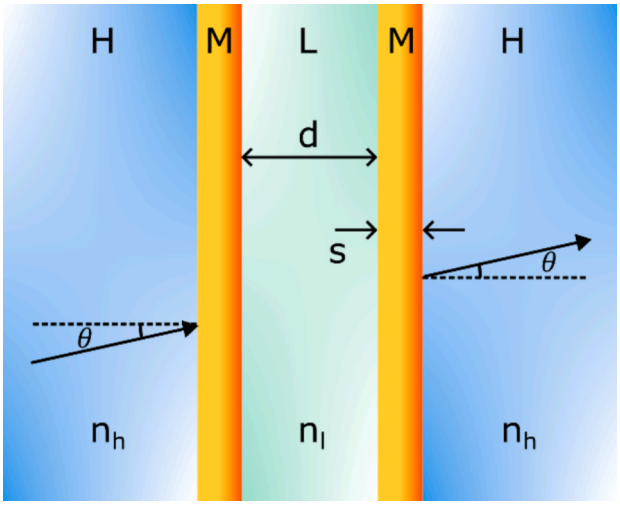

Fig. 1. Schematic drawing of an HMLMH optical structure.

The refractive index inequality, $n_h > n_l$, allows the incidence angle to exceed the critical value $\theta_{cr} = \sin^{-1}(n_l/n_h)$. In the case of $\theta > \theta_{cr}$, there is an evanescent wave inside the cavity. This allows light coupling to different types of resonances within the structure, resulting in its transmission through the multilayer for incidence angles under which light would not have been expected to reach the other side, thus leading to a resonant optical tunnelling process [28–30].

This atypical transmittance can be analytically modelled using Fresnel coefficients iteratively at each of the interfaces and considering the propagation of electromagnetic fields through each of the layered media [31,32]. Besides, plasmonic resonances are associated with charge oscillations at the interface of metallic and dielectric media, requiring a non-null field component in the direction normal to these interfaces, which are transverse magnetic (TM) or p-polarised waves. Therefore, only TM waves must be considered. Generalised Fresnel formalism leads to the following expressions for the reflection and transmission amplitude coefficients of the whole system:

$$r_{h/h} = r_{hml} + \frac{t_{hml}t_{lmh}r_{lmh}e^{i2k_{l\perp}d}}{1 - r_{lmh}^2 e^{i2k_{l\perp}d}} = \frac{r_{hml} + a_{lmh}r_{lmh}e^{i2k_{l\perp}d}}{1 - r_{lmh}^2 e^{i2k_{l\perp}d}}$$
$$t_{h/h} = \frac{t_{hml}t_{lmh}e^{ik_{ln}d}}{1 - r_{lmh}^2 e^{i2k_{l\perp}d}} \quad (1)$$

where h/h is an abbreviation for *hmlmh*. Furthermore, [31,33]:

$$a_{lmh} = a_{hml} = t_{lmh}t_{hml} - r_{lmh}r_{hml} = \frac{e^{i2k_{l\perp}d} + r_{mh}r_{ml}}{1 - r_{mh}r_{ml}e^{i2k_{l\perp}d}} \quad (2)$$

The three subindices of each coefficient in the previous formula account for the three-layered media faced by the incident electromagnetic radiation. The reflection (transmission) amplitude coefficient r_{ijk} (t_{ijk}) corresponds to a wave arriving from medium "i" towards medium "k", with the medium "j" between those two. $k_{l\perp}$ is the normal component of the wavevector inside the cavity (within medium L), which can be calculated from the refractive indices and the incidence angle using the following formula:

$$k_{l\perp} = k_0\sqrt{n_l^2 - n_h^2\sin^2\theta} \quad (3)$$

Given the expression for the critical incidence angle, it is clear that $k_{l\perp}$ is real for $\theta < \theta_{cr}$ and pure imaginary for $\theta > \theta_{cr}$ (only evanescent waves are allowed within the inner medium then). In any case, r_{imk} and t_{imk} coefficients used in Eq. (1) define the optical properties of the two cavity mirrors, representing amplitude reflection and transmission either from outside (r_{hml} and t_{hml}) or from inside (r_{lmh} and t_{lmh}) the cavity. These can

be expressed in terms of the TM Fresnel coefficients associated with the single metal-dielectric interfaces as follows:

$$r_{imj} = \frac{-r_{mi} + r_{mj}e^{i2k_{m\perp}s}}{1 - r_{mi}r_{mj}e^{i2k_{m\perp}s}}; \qquad t_{imj} = \frac{t_{im}t_{mj}e^{ik_{m\perp}s}}{1 - r_{mi}r_{mj}e^{i2k_{m\perp}s}} \tag{4}$$

where s represents the thickness of each metallic mirror. $k_{m\perp}$ is the normal component of the wavevector inside the metal and is given as follows:

$$k_{m\perp} = k_0\sqrt{n_m^2 - n_h^2\sin^2\theta} \tag{5}$$

The last terms in Eqs. (3) and (5) are equal because the component of the wavevector parallel to the interfaces is invariant under propagation in the system, $\beta = k_0 n_h \sin\theta$. The TM Fresnel coefficients for incidence at a single interface from medium "i" towards medium "j" are given as follows:

$$r_{ij} = \frac{\varepsilon_j k_{i\perp} - \varepsilon_i k_{j\perp}}{\varepsilon_j k_{i\perp} + \varepsilon_i k_{j\perp}} t_{ij} = \sqrt{\frac{\varepsilon_i}{\varepsilon_j}}(1 + r_{ij}) \tag{6}$$

and the relative electrical permittivity in medium "i" is $\varepsilon_i = n_i^2$. Considering all the above, one can square the modulus of Eq. (1) to obtain the transmittance of the cavity, $T = |t_{h/h}|^2$. This formula is well known when considering small incidence angles; however, the novelty lies in its generalisation for angles greater than the critical angle θ_{cr} between the two dielectric media, which is given as follows:

$$T = \frac{|t_{lmh}t_{hml}|^2}{4\rho_{lmh}^2\left[\sinh^2\left(k''_{l\perp}d - \ln\rho_{lmh}\right) + \sin^2\left(k'_{l\perp}d + \varphi_{lmh}\right)\right]} \tag{7}$$

with $r_{lmh} = \rho_{lmh}e^{i\varphi_{lmh}}$, and the normal component of the wavevector is split into its real and imaginary parts, $k_{l\perp} = k'_{l\perp} + ik''_{l\perp}$. The previous formula shows a relatively straightforward dependence on the intra-cavity thickness d, but more complex dependencies on both the incidence angle θ and wavelength λ. Nevertheless, extracting some relevant information is still feasible.

Fig. 2 shows a typical transmittance map plotted as a function of incidence angle and wavelength for a cavity with a fixed thickness. The different curves or branches that appear on the map correspond to resonances of the cavity, which are defined by the condition of maximum transmittance. This definition is essential, since the location of reflectance minima is slightly shifted because of its dependence on the reflection coefficient r_{hml}, which does not influence the transmittance. There are two main types of resonances. First, for incidence angles below the critical angle ($\theta < \theta_{cr}$), photonic or volume resonances, involving harmonic waves, occur [27]. These are Fabry–Perot type resonances for very thin cavities. Second, above the critical incidence ($\theta > \theta_{cr}$) surface resonances, which are plasmonic as they are associated with the creation of charge density oscillations at the dielectric-metal interfaces, are observed. The plasmonic resonances involve high electric fields at both ML interfaces inside the cavity, which means CSP resonances. Field distributions demonstrating the plasmonic character of these resonances are provided in the supplementary material. Fig. 2 shows the merging of these resonances into a single resonance, from where the transmittance gradually vanishes. Moreover, the lower of the plasmonic resonances matches the first of the photonic resonances at the critical angle. All these resonances and their behaviours resemble the permissible modes in an MDM structure with semi-infinite metals [34,35]. Fig. 2b shows experimental results confirming the theoretical prediction in Fig. 2a. Further details are given in Section 6.

This first example is presented as an overview of the output of the microcavity. Next, to start a thorough analysis of its transmission, we first consider a fixed wavelength and the simplest ideal case, where the permittivity of the metal is purely real.

3. CSP resonances in ideal lossless metals

As mentioned above, the photonic or volume resonances, allowed for incidence angles below θ_{cr}, correspond to the same well-known physical phenomenon as those in a Fabry–Pérot interferometer. For this reason, in the theoretical analysis, we focus on the CSP resonances in the cavity, corresponding to incidence angles such that $\theta > \theta_{cr}$, which is the angular range considered from now on. In this case, $k_{l\perp}$ is purely imaginary, and Eq. (7) is therefore simpler and can be given as follows:

$$T = \frac{|t_{lmh}t_{hml}|^2}{4\rho_{lmh}^2\left[\sinh^2\left(k''_{l\perp}d - \ln\rho_{lmh}\right) + \sin^2(\varphi_{lmh})\right]} \qquad \theta > \theta_{cr} \tag{8}$$

We first consider the ideal case in which the permittivity of metals follows the Drude's model without losses and is thus real.

$$\varepsilon_m = 1 - \left(\omega_p/\omega\right)^2 \tag{9}$$

Spectral variations are not considered at this stage; therefore, the frequency is fixed at $\omega = \omega_0$, which is lower than the plasma frequency ω_p. This condition, $\omega_0 < \omega_p$, implies that the real part of the permittivity of the metal is negative, that is, $\varepsilon_m = \varepsilon'_m < 0$. Otherwise, for frequencies above the plasma value, both materials have positive permittivity, and plasmons are not allowed. Given that $\varepsilon_m = n_m^2$, choosing a frequency below ω_p implies a purely imaginary refractive index, that is, $n_m = in''_m$. Together with Eq. (5), this implies $k_{m\perp} = ik''_{m\perp}$. Consequently, from Eq. (6), we get $\rho_{mh} = 1$, and r_{ml} is real and greater than unity. This unusually high value of the Fresnel reflection coefficient between the mirrors and the inner medium leads in Eq. (4) to high ρ_{lmh} values, which appear in Eq. (8), and are responsible for the resonant transmission maxima when

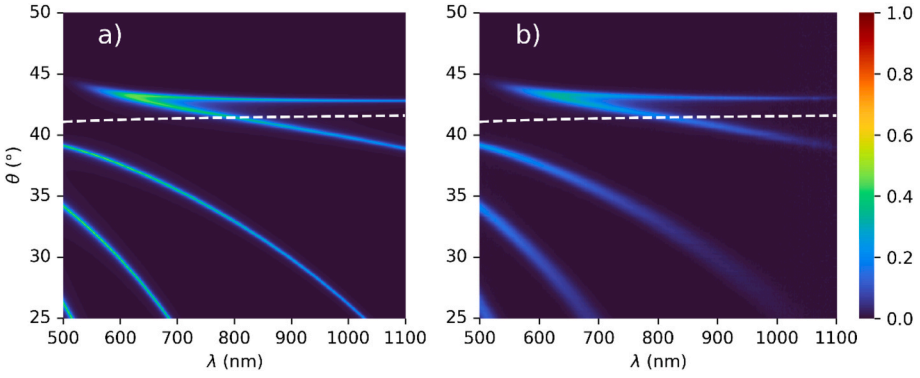

Fig. 2. Example of transmission resonances in an optical microcavity with silver mirrors (M) separated by a thin air gap (L) and surrounded by BK7 glass (H). a) Theoretical results with $d = 1250nm$ and $s = 45nm$ b) Experimental results are shown for comparison (see Section 6. Experimental, for details). The white dotted line corresponds to the critical angle curve $\theta_{cr}(\lambda)$.

the incident energy couples to CSPs. This is discussed in the next Section.

Since the system is transparent, the energy flow in the cavity must match the transmitted flow. In this situation, $|t_{lmh}|^2 = \left|\frac{k_{ln}}{k_{hn}}\left(r_{lmh} - r^*_{lmh}\right)\right|$. This equality, together with the relation $k_{h\perp}t_{lmh} = k_{l\perp}t_{hml}$ [31], leads to $|t_{lmh}t_{hml}|^2 = 4|r_{lmh}|^2\sin^2(\varphi_{lmh})$. Therefore, the expression of transmittance in Eq. (8) can be rewritten into a simplified version for incidence angles above the critical angle as follows:

$$T = \frac{1}{1 + \left[\frac{\sinh\left(k''_{l\perp}d - \ln\rho_{lmh}\right)}{\sin(\varphi_{lmh})}\right]^2} \tag{10}$$

According to this equation, the transmittance of the microcavity reaches a maximum value of one if the hyperbolic sine vanishes, which can be written as follows:

$$d = \frac{1}{k''_{l\perp}}\ln\rho_{lmh} = \frac{1}{k_0\sqrt{n_h^2\sin^2\theta - n_l^2}}\ln\rho_{lmh}(\theta) \equiv H(\omega_0,\theta) \equiv F(\theta) \tag{11}$$

This condition expresses the existing constraint between the incidence angle and the cavity thickness that can only be fulfilled if $\rho_{lmh} > 1$. In general, there are two CSP resonances that are solutions of Eq. (11), corresponding to two different continuous curves in the (θ, d) plane (Fig. 3a). The first, located at higher incidence angles, starts at $\theta = 90^\circ$ for its minimum value of $d = F(90^\circ)$, whereas the second begins at the critical angle (limit of the considered angular region) for its minimum intracavity thickness $d = F(\theta_{cr})$, From those points, the two resonance curves converge to a common value of d, $d_{max} \equiv d_{co} = F(\theta_{co})$, at an intermediate angle $\theta = \theta_{co}$. (θ_{co}, d_{co}) denote the coalescence angle and coalescence thickness, corresponding to the common values at which both CSP resonance curves meet. d_{co} is the maximum value of the intracavity thickness that verifies Eq. (11). However, T can still have maxima at $\theta = \theta_{co}$ for thicker cavities ($d > d_{co}$) despite not reaching $T = 1$; therefore, they must be considered as continuation of the resonance.

By comparing the CSP radiative resonance with the modes of an MDM structure [35], it can be shown that the CSP at higher incidence angles corresponds to the fundamental resonance TM_0, that already appears for small cavity thicknesses and has a symmetric magnetic field distribution across the structure (the distribution is also symmetric for the component of the electric field normal to the interfaces). The other CSP presents an antisymmetric magnetic field distribution and corresponds to the TM_1 resonance. As usual, the order of the resonance increases as the value of the invariant β defined previously in Section 2 decreases.

Fig. 3a shows the curve of maximum transmittance in the (d, θ) plane for incidence angles above the critical angle. The two resonant solutions coalesce at (d_{co}, θ_{co}) and become degenerated for greater cavity thicknesses, producing a single observable maximum in transmittance at that same incident angle θ_{co}. Fig. 3b shows the maximum transmittance values for various cavity thicknesses. Full transmission takes place even through cavities with thicknesses of several wavelengths. Over the coalescence thickness, the transmittance maximum $T_{max} = T(d, \theta_{co})$ decreases gradually towards 0 because the hyperbolic sine in Eq. (10) increases. The transmittance curve can be divided into three distinct regions: i) zone of full transmission, $d < d_{co}$, where $T_{max} = 1$; ii) zone of FTIR with moderate transmission, $d \gtrsim d_{co}$, where $T_{max} = T(d, \theta_{co}) < 1$; iii) zone of FTIR with low exponentially decreasing transmission, $d - d_{co} \gg 1/k''_{l\perp}$, where $T_{max} = T(d, \theta_{co}) \cong \sin^2(\varphi_{lmh})e^{-2k''_{l\perp}(d-d_{co})} \ll 1$. The limit $T_{max} = 0$ corresponds to TIR. This curve can be compared with the corresponding one for FTIR in dielectric materials [36]. In this case, the transmittance is obtained from Eq. (10) making the substitution $r_{lmh} \to r_{lh}$. Since $\rho_{lh} = 1$, it necessarily implies that $\ln\rho_{lh} = 0$ and a region of full transmission is not present in FTIR. However, the behaviour is similar in the two other regions.

4. CSP resonances in lossy metals

A non-ideal case implies considering a real metal having a complex dielectric constant, with a non-zero imaginary part, accounting for absorption. However, its negative real part is still considered to be significantly higher in magnitude, that is, $\varepsilon = \varepsilon' + i\varepsilon''$, where $-\varepsilon' \gg \varepsilon'' > 0$. This last inequality is true for most plasmonic materials in the infrared–visible spectral region and is commonly used in the modelling of plasmonic phenomena. Introducing losses in the Drude model leads to the following expression for relative permittivity, which is used in Table 1 to model the permittivity for some metals:

$$\varepsilon_m = 1 - \frac{\omega_p^2}{\omega^2 + i\omega\Gamma} \tag{12}$$

The most significant change in transmittance in comparison with the previous ideal case is that the absorption at the metallic mirrors causes a

Table 1
Plasma frequency and damping constant for different metals [37] and the resulting permittivity values at visible and infrared wavelengths.

Material	$\omega_p(s^{-1})$	$\Gamma(s^{-1})$	ε	
			$\lambda = 600nm$	$\lambda = 1000nm$
Silver	1.369×10^{16}	2.730×10^{13}	$-18.013 + 0.165i$	$-51.807 + 0.765i$
Gold	1.371×10^{16}	4.040×10^{13}	$-18.067 + 0.245i$	$-51.948 + 1.136i$
Copper	1.122×10^{16}	1.378×10^{13}	$-11.772 + 0.056i$	$-34.476 + 0.260i$
Aluminium	2.240×10^{16}	1.242×10^{14}	$-49.827 + 2.011i$	$-139.796 + 9.283i$
Nickel	7.419×10^{15}	6.626×10^{13}	$-4.582 + 0.118i$	$-14.493 + 0.545i$

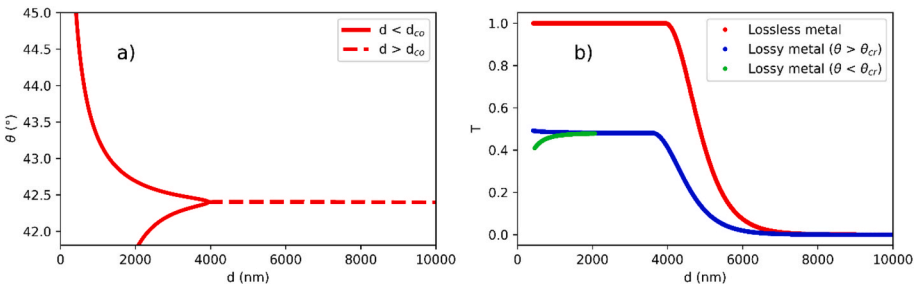

Fig. 3. In red, resonance curve and its transmittance for an ideal lossless metal with permittivity given by Eq. (9) with $\lambda = 1\mu m$ and $\omega_p = 1.35{\cdot}10^{16}s^{-1}$, $n_h = 1.5$ and $n_l = 1$. The red dotted line shows the degenerated resonance line at which both TM_0 and TM_1 resonances have coalesced for thicknesses greater than the coalescence thickness d_{co}. For comparison, resonant transmittance in a lossy metal ($\Gamma = 6{\cdot}10^{13}s^{-1}$) is also shown. The blue line in (b) corresponds to the two plasmonic resonances, while the green line corresponds to the TM_1 resonance in the photonic regime. Before the coalescence distance, the two plasmonic resonances have similar but slightly different transmittance, which is greater for the fundamental one, and becomes degenerated at d_{co}.

reduction in the fraction of energy that is transmitted through the microcavity, as shown in Fig. 3b. In this case, Eq. (10) is no longer valid; however, transmittance can be written as follows:

$$T = \frac{T_0}{1 + \left[\frac{\sinh\left(k_{l\perp}'' d - \ln\rho_{lmh}\right)}{\sin(\varphi_{lmh})}\right]^2}; \quad T_0 = \left[\frac{|t_{lmh}t_{hml}|}{2\rho_{lmh}\sin(\varphi_{lmh})}\right]^2 \tag{13}$$

This equation is similar to Eq. (10), except for a multiplicative common factor that accounts for the decrease in T due to absorption, $T_0(\theta) \leq 1$, that depends on the incidence angle. The independence of T_0 with respect to the intracavity thickness d implies that Eq. (11) is valid for the location of transmittance maxima in d for each fixed incidence angle. Besides, it is still an excellent approximation for the position of transmittance maxima in θ for a constat cavity thickness. Fig. 4 shows two examples of the good agreement of the prediction of Eq. (11) for the position of the resonances and results of a computation of transmittance using non-ideal metals.

Thus, for pairs of values (d, θ) that verify Eq. (11), the maximum value of transmittance is $T_{max} = T_0(\theta) \leq 1$. Fig. 3b shows the decrease in the fraction of transmitted light at resonances with respect to the ideal case. High transmittance maxima at the resonances occurs when ρ_{lmh} is small (but larger than one), which occurs for thin metallic layers or for low refractive index contrasts (between the real part of n_m and n_l). Moreover, it should be noted from Eq. (11) that smaller ρ_{lmh} values imply thinner coalescence. Similar to that for lossless metals, we divide the transmission curve at resonance in three zones: i) $d \leq d_{co}, T_{max}(d, \theta) = T_0(\theta) < 1$, optimal but different transmission for the two CSP resonances, and higher for the fundamental one; ii) $d \gtrsim d_{co}$, $T_{max} = T(d, \theta_{co}) < T_0(\theta_{co})$, attenuated optical tunnelling (AOT) with moderate transmission; iii) $d - d_{co} \gg 1/k_{l\perp}'', T_{max} \cong T_0(\theta_{co})\sin^2(\varphi_{lmh})e^{-2k_{l\perp}''(d-d_{co})} \ll 1$, AOT with low exponentially decreasing transmission. The limit of this region is ATR but, in practice, this limit is reached when d exceeds d_{co} in some unities of $1/k_{l\perp}''$. Moreover, the existence of region i) implies that $\rho_{lmh} > 1$.

As mentioned above, the coefficient r_{lmh} plays a relevant role in the appearance of resonances. Fig. 5 shows the angular dependence of the reflection coefficient r_{lmh} when varying different parameters of the metallic mirrors. From Eq. (4), we have the following:

$$r_{lmh} = \frac{-r_{ml} + r_{mh}e^{i2k_{m\perp}s}}{1 - r_{ml}r_{mh}e^{ik_{m\perp}s}} \tag{14}$$

The modulus of r_{lmh}, shown in the subplots on top in Fig. 5, increases around the coalescence angle θ_{co}, reaching values significantly greater than unity. The peak of ρ_{lmh} coincides with a phase jump, and the slope of φ_{lmh} is maximum at that same angle in the corresponding subfigures. As shown in Fig. 5a and 5b, increasing the imaginary part of the permittivity reduces the maximum values of the modulus and the slope of the phase, but with little change in the position of the curves. Fig. 5c and d show the effect of varying the real part of the dielectric constant. An increase in the absolute value of ε' leads to an increment of both the maximum value of ρ_{lmh} and maximum slope of φ_{lmh}, as well as a shift of both curves towards lower angles. Finally, as shown in Fig. 5e and f, increasing the metal mirror thickness shows a trend similar to that in the previous case, but more moderate. It can be pointed out that as $s \to \infty$, $r_{lmh} \to r_{lm}$, which corresponds to the highest possible value of ρ_{lmh} and the greatest slope of φ_{lmh}.

These changes in coefficient r_{lmh} translate into changes in transmission at resonance. The decrease in the maximum values of transmittance (T_0) are more drastic for higher values of the imaginary part of the permittivity (Fig. 7b). Moreover, the coalescence thickness and angle shift slightly towards lower values with the increase in the imaginary part (Fig. 7a). We can consider the curves obtained for $|\varepsilon''/\varepsilon'| \leq 10^{-3}$ to be very close to those for a lossless metal.

In contrast, varying the real part of the permittivity while its imaginary part is kept constant leads to a different behaviour. Maximum transmittance increases with decreasing absolute values of the real permittivity because of a decrease in ρ_{lmh}. Changes in coalescence thickness and angle are more important than those in transmittance (Fig. 6c and d), particularly when compared with the previous case where variations occurred in the imaginary part. Regarding changes in transmittance as a function of the mirror thickness, s, (Fig. 6e and f), d_{co} increases with increasing s (ρ_{lmh} increases), whereas θ_{co} and T_0 decrease. Therefore, for an optimal microcavity a balance between higher coalescence thickness and maximum transmittance must be maintained.

5. Spectral resonance curves

We now examine the case with a constant incidence angle and varying wavelengths to study the spectral variation of resonances. In this case, the resulting (d, λ) map is drastically different depending on the angular region where the fixed angle, $\theta = \theta_0$, lies. For plasmonic resonances to be observed at any wavelength λ, $\theta_0 > \theta_{cr}(\lambda)$ must be verified. Furthermore, we have a TM_1 resonance in the plasmonic regime for wavelengths where $\theta_{cr}(\lambda) < \theta_0 < \theta_{co}(\lambda)$, in which $\theta_{co}(\lambda)$ is the curve that defines the coalescence angle as a function of wavelength. Finally, we have a TM_0 resonance when $\theta_0 > \theta_{co}(\lambda)$. Fig. 7a shows the regions where the different resonances are observed in a (λ, θ) map, and Fig. 7b and c show the resonance curves corresponding to two different fixed values of θ_0 in a (λ, d) map.

In any case, the plasmonic resonances must verify the resonant condition equivalent to that observed in the angular case (Eq. (11)). That means

$$d = \frac{1}{k_{ln}''}\ln\rho_{lmh} \equiv H(\lambda, \theta_0) = G(\lambda) \tag{15}$$

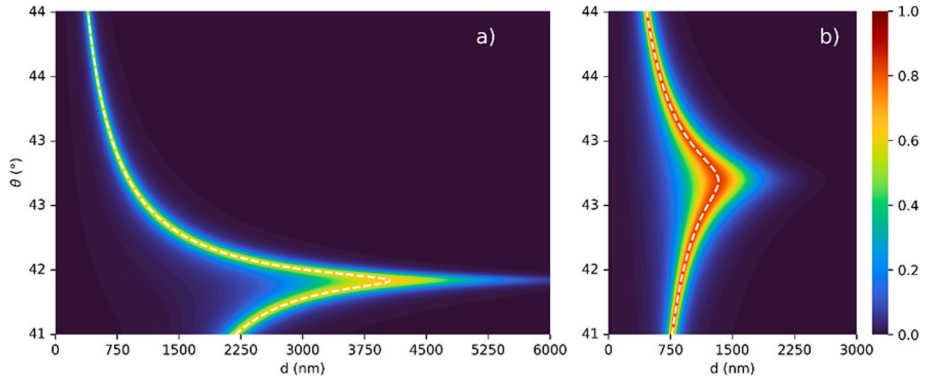

Fig. 4. Transmittance in the (d, θ) plane with $\omega_p = 1.5{\cdot}10^{16}s^{-1}$ and $\Gamma = 3{\cdot}10^{13}s^{-1}$ a) $\lambda = 1\mu m$ b) $\lambda = 0.6\mu m$ The white dashed lines correspond to the resonance predicted by Eq. (11).

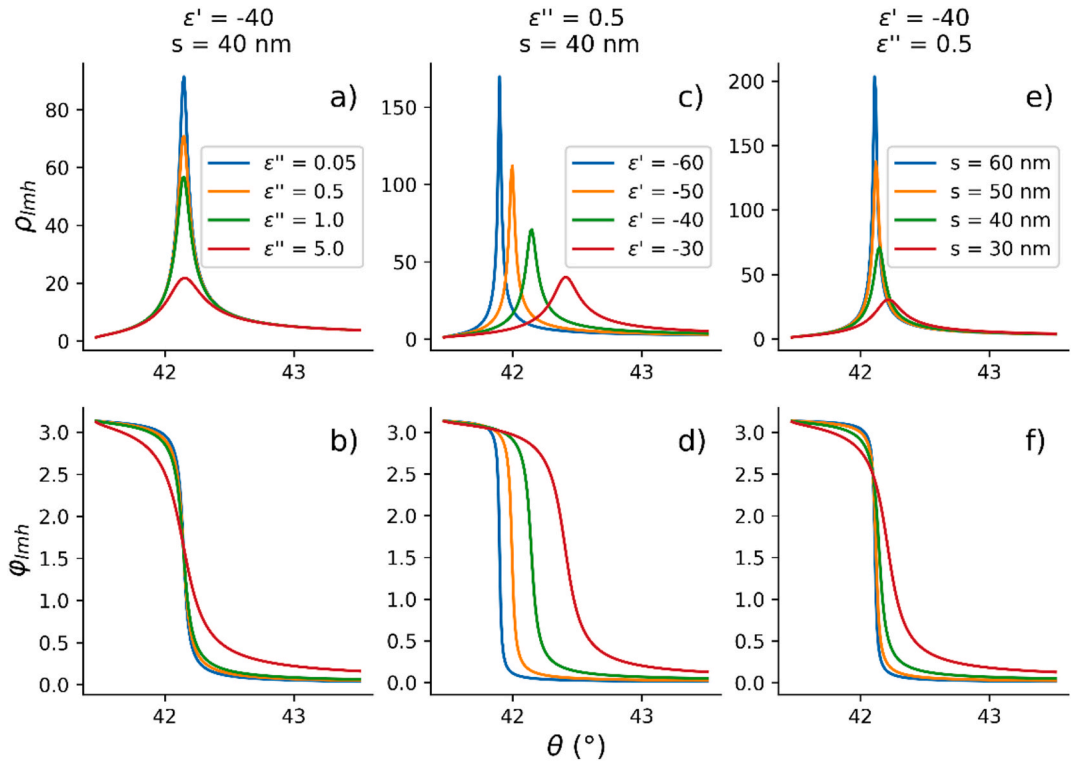

Fig. 5. Modulus ρ_{lmh} (top) and phase φ_{lmh} (bottom) of the reflection coefficient r_{lmh} varying different parameters of the metallic layers ε'' (a, b), ε' (c, d) and thickness s (e, f). λ is set to 1000 *nm*.

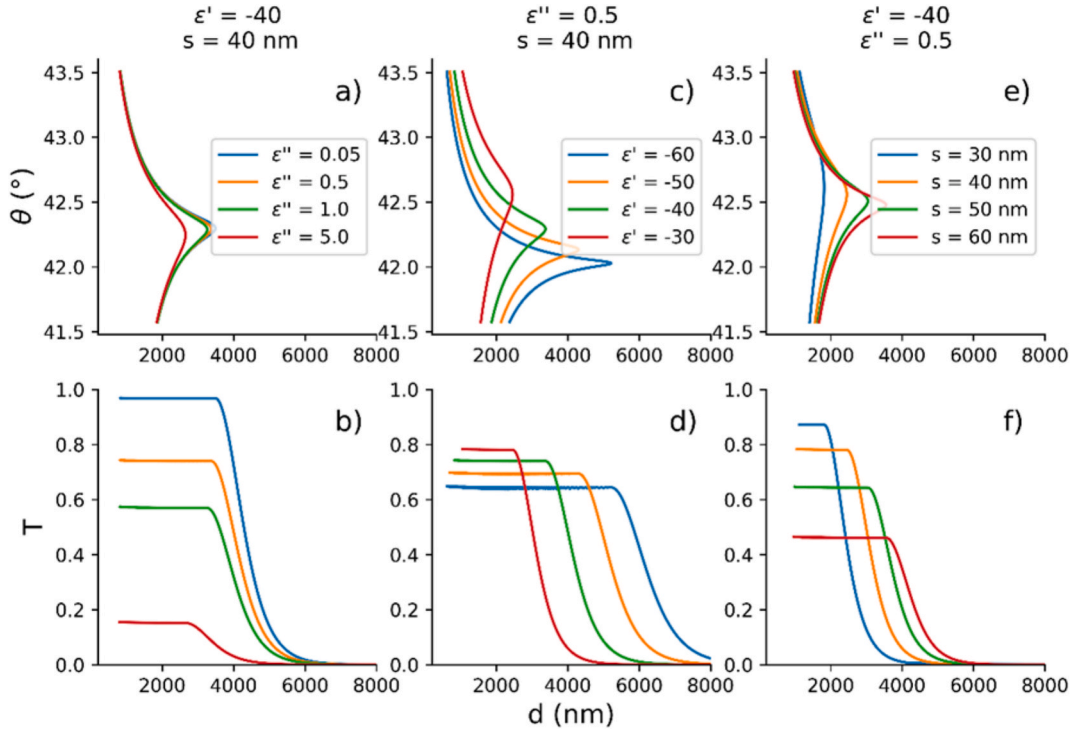

Fig. 6. Resonance curve (top) and transmittance at resonance (bottom) varying different parameters of the metallic layers ε'' (a, b), ε' (c, d) and thickness s (e, f).

Thus, depending on the chosen fixed incidence angle, this condition might have two, one or no solutions for different wavelengths in the considered spectral range. In contrast, let us consider the resonance curves $d = H(\lambda, \theta)$. The curves plotted in Fig. 7d are obtained using the lossy version of the Drude model and the contour plot allows tracking of the position of the resonance along the three variables. The maxima on the plasmonic branches shown in Fig. 2 correspond to one of these curves. For a given thickness, corresponding to any of the curves shown in the figure, the fundamental CSP resonance is located at higher angles and wavelengths and converges with the TM_1 resonance at the

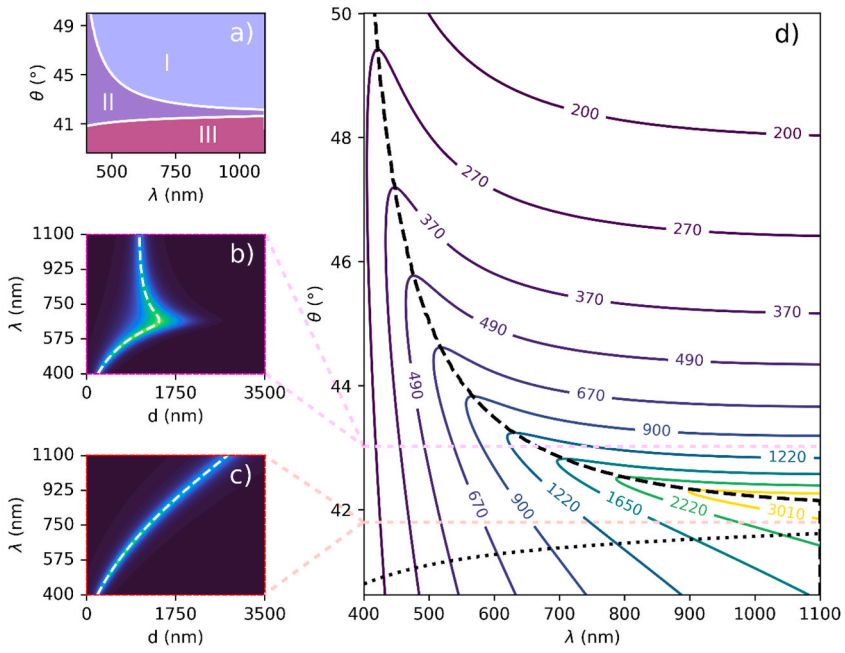

Fig. 7. (a) Diagram showing the locus of resonances. Region I corresponds to TM_0 resonance; region II to TM_1 resonances in the plasmonic regime and region III to photonic resonances (TM_n, $n > 1$). The upper continuous white line corresponds to the spectral coalescence curve $\theta_{co} = f(\lambda)$, and the lower one represents the spectral critical angle curve $\theta_{cr} = g(\lambda)$. Spectral transmittance for two different incident angles, $\theta = 43^o$ (b) and $\theta = 41.76^o$ (c). The dashed white line corresponds to the resonant condition (15). (d) Map of resonance using the lossy Drude model, Eq. (12), with $\omega_p = 1.25{\cdot}10^{16}s^{-1}$, $\Gamma = 8.1{\cdot}10^{13}s^{-1}$. The metal thickness is $s = 45nm$.

coalescence curve, $\theta_{co} = f(\lambda)$ (the black dotted line), as can be deduced from Fig. 7a. The thicker the cavity, the longer the wavelength and the smaller the angle for which the coalescence curve is reached. Furthermore, the ratio between d_{co} and wavelength increases with the wavelength. For example, $d_{co} \sim \lambda$ for a wavelength around 500 nm, $d_{co} \sim 2\lambda$ for a wavelength around 700 nm, and $d_{co} \sim 3\lambda$ for a wavelength around 900 nm.

The data shown in Fig. 7d is analysed through several interesting cuts. Thus, vertical lines correspond to slices of the graph for a constant wavelength and are associated to transmittance maxima as those shown in Fig. 4. Horizontal slices correspond to spectral variations for a fixed angle of incidence and are associated to transmittance maxima as those shown in Fig. 7b and c.

6. Experimental

To validate the results presented in the previous sections, we conducted experimental measurements under selected configurations and compared them with the theoretical prediction. The experimental setup is illustrated in Fig. 8, which shows the two configurations used: (a) constant wavelength analysis at different angles and thicknesses; (b) spectral/angular analysis at a fixed intracavity thickness. To achieve angles of incidence higher than the critical angle we use prism coupling and a similar decoupling prism to measure the system transmission. The prisms are made of BK7 glass and have a thin silver layer on their hypotenuses deposited using a PVD chamber BA 510 by Balzers. Layer thicknesses were measured with a needle profilometer (model Dektak 3 from Veeco Metrology), yielding results consistent with the nominal values given by the deposition system.

NKT Supercontinuum source was used as the light source. Spectral measurements were performed with a custom-built grating spectrometer with a spectral range from 550 to 1050 nm and resolution of 0.5 nm/pixel. A photodiode sensor (Thorlabs S130C) and different spectral filters were used to collect the transmitted light signal at constant wavelengths. Another photodiode controlled the incident power for reference. After selection of TM polarization with a polarizing beam splitter, we slightly focused the light on the air gap between the prisms.

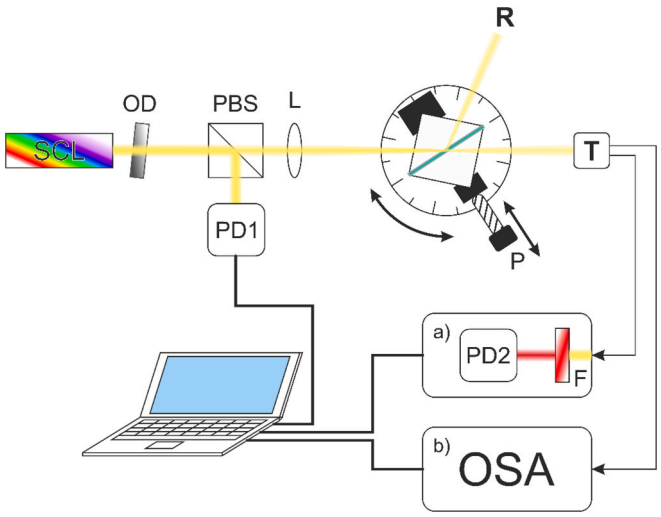

Fig. 8. Schematic of the experimental setup used for θ-d (a) and spectral/angular (b) analysis. SCL supercontinuum source, OD optical density, PBS polarizing beam splitter, L converging lens, P piezoelectric actuator, F spectral filter, PD photodiode.

For angular positioning and control, we used a rotation platform (model URS75BCC from Newport Optics). The two prisms were aligned in a 3D-printed capsule and brought closer using a Thorlabs PIAK25 piezoelectric actuator, which allowed precise displacement steps of approximately 20 nm/step.

A comparison between simulated and experimental transmittance with an air gap of constant thickness is presented in Fig. 2. The main difference between theory and experiment is a reduction in peak prominence and broadening of the resonance peaks in the experimental data, particularly as the peaks shift away from the coalescence point. A similar trend is observed for other cavity thicknesses.

Fig. 9(a–c) show transmittance measurements over an angular range

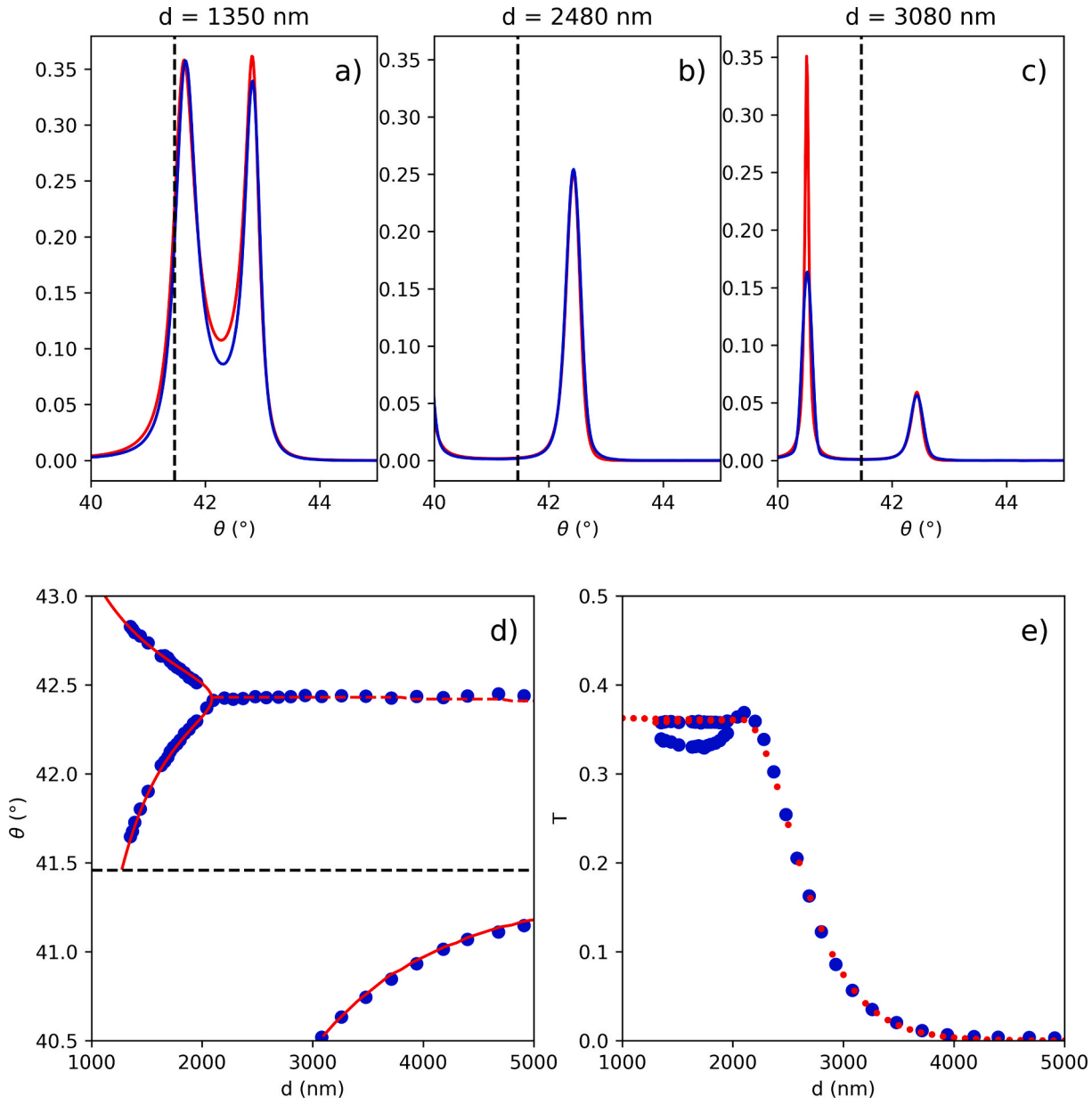

Fig. 9. Experimental measurement taken at $\lambda = 800nm$ and s $\simeq$ 39 nm. (a)-(c) Transmittance versus incidence angle at three different cavity thicknesses (d). Resonant angles for different thickness and their peak transmittance (e). Blue lines and dots are experimental values, while red ones correspond to theoretical predictions. The dashed black line corresponds to the critical angle.

from 40° to 45° at a fixed wavelength $\lambda = 800$ nm for a similar BK7-silver-air structure, and three different intracavity thicknesses. The thicknesses in 9(b) and 9(c) are greater than the coalescence distance d_{co}, whereas the one in 9(a) is smaller. In 9(a), the two CSP resonances are resolved and exhibit optimal transmission; in 9(b), only a degenerate CSP resonance with moderate transmission is observed; in 9(c), a photonic resonance is observed together with the degenerate CSP resonance with low transmission. Fig. 2 illustrates that the experimental and simulated transmissions differ more below the critical angle.

Fig. 9(d–e) display the evolution of the angular position of resonances and their transmittances as the cavity is gradually closed using the piezo actuator, until a minimum achievable spacing of approximately 1300 nm. The curves shown in Fig. 9d represent the resonance peak positions in a (d, θ) map for plasmonic and first full photonic (TM_2) resonances. Fig. 9e shows the transmittance values for the plasmonic resonances.

These results demonstrate a good agreement between experimental and simulated data. The traceability of individual peaks allows for a clear comparison. In Fig. 9d, the coalescence of the two CSPs is visible, along with the emergence of the first full photonic resonance. It is necessary to point out that the permittivity of noble metals varies with film thickness at the nanometre scale [38]. Thus, the values used in our simulations for silver are fitted to match the experimental data, rather than taken directly from the literature. Nonetheless, the fitted values are consistent with previously reported values [39,40] for the considered wavelength (see Table 2).

Table 2
Value of real and imaginary parts of the dielectric constant of silver.

Silver dielectric constant at 800 nm	ε'	ε''
20 nm thick film [39]	−27.1589	0.9798
Bulk [40]	−28.7300	1.9165
Our simulation	−28.6198	1.5085

7. Conclusions

In this work, we conducted a detailed theoretical study of CSP resonances in symmetric MLM optical microcavities surrounded by a high-index medium (H). Starting from a generalized multi-beam interference model for three-layer systems, we extend it into the plasmonic regime where the inner wave was evanescent at high incidence angles because of total internal reflection. This permits the definition of a clear resonance condition for high transmittance through the cavity, under conditions where strong reflection would be expected.

CSP resonances, which arise from coherent oscillations at both metal-dielectric interfaces, gave rise to resonant optical tunnelling. We derived and verified resonance conditions, including coalescence thickness and angle, which marked the point at which the two distinct CSP resonances degenerated into a single transmission peak. These phenomena were first analysed for lossless ideal metals and then extended to real lossy metals. Including realistic material parameters revealed how losses limited transmission efficiency, but did not invalidate the resonance conditions at over-wavelength thicknesses. In the study, the relevance of the amplitude coefficient r_{lmh} was recognised.

We complemented our theoretical findings with experimental measurements using an all-custom-built setup. The results, obtained by precisely controlling cavity thickness and monitoring transmittance at varying wavelengths or incidence angles, were in excellent agreement with the results of theoretical simulations. Key phenomena such as AOT and resonant coalescence were observed as predicted.

These findings reinforce the potential of CSP-based microcavities for applications in highly selective optical filtering, sensing, and nanoscale light manipulation. Moreover, the simple analytical condition for resonance positioning could be a valuable tool for designing practical plasmonic devices operating in the visible and near-infrared spectral regions.

The present manuscript fills a gap in the field of plasmonics, presenting an analytical model of transmission in the plasmonic regime for a simple optical microcavity with thin-film metallic mirrors. Despite the strong reflective properties of metals in the visible spectrum and total internal reflection at the first mirror under normal conditions, resonant coupling of light between the two mirrors (CSP excitation) enables the light to tunnel through the structure. This results in a high transmission across a range of supra-wavelength cavity thicknesses, limited primarily by absorption in the metallic layers. The phenomenon remarkably exemplifies optical tunnelling. We believe these results can be extended in further studies to similar but alternative microcavities, including those with asymmetric configurations.

CRediT authorship contribution statement

Alejandro Doval: Writing – review & editing, Writing – original draft, Software, Investigation. **Yago Arosa:** Writing – review & editing, Methodology, Investigation. **Raúl de la Fuente:** Writing – review & editing, Supervision, Methodology, Investigation, Conceptualization.

Declaration of competing interest

The authors declare that they have no known competing financial interests or personal relationships that could have appeared to influence the work reported in this paper.

Acknowledgements

AD would like to thank Ministerio de Universidades, Spain for the financial support through FPU21/01302. YA acknowledges the funding from the postdoctoral fellowship ED481D-2024-001 from Xunta de Galicia, Spain. This research was funded by the project USC 2024-PU031 from the University of Santiago de Compostela, Spain and GRC ED431C 2024/06 from Xunta de Galicia, Spain.

Appendix A. Supplementary material

Supplementary data to this article can be found online at https://doi.org/10.1016/j.optlastec.2025.113602.

Data availability

Data will be made available on request.

References

[1] R.H. Ritchie, Plasma losses by fast electrons in thin films, Phys. Rev. 106 (1957) 874–881.
[2] T. Turbadar, Complete absorption of light by thin metal films, Proc. Phys. Soc. 73 (1959) 40.
[3] K.R. Welford, J.R. Sambles, Coupled surface plasmons in a symmetric system, J. Mod. Opt. 35 (1988) 1467–1483.
[4] E.N. Economou, Surface Plasmons in thin films, Phys. Rev. 182 (1969) 539–554.
[5] R. Dragila, B. Luther-Davies, S. Vukovic, High transparency of classically opaque metallic films, Phys. Rev. Lett. 55 (1985) 1117–1120.
[6] J.J. Burke, G.I. Stegeman, T. Tamir, Surface-polariton-like waves guided by thin, lossy metal films, Phys. Rev. B 33 (1986) 5186–5201.
[7] J. Homola, M. Piliarik, Surface Plasmon Resonance (SPR) Sensors, in: J. Homola (Ed.), *Surface Plasmon Resonance Based Sensors*, Springer, Berlin, Heidelberg, 2006, pp. 45–67, https://doi.org/10.1007/5346_014.
[8] E. Kretschmann, Die Bestimmung optischer Konstanten von Metallen durch Anregung von Oberflächenplasmaschwingungen, Z. Physik 241 (1971) 313–324.
[9] A. Otto, Excitation of nonradiative surface plasma waves in silver by the method of frustrated total reflection, Z. Physik 216 (1968) 398–410.
[10] Y. Akimov, Optical resonances in Kretschmann and Otto configurations, Opt. Lett. 43 (2018) 1195–1198.
[11] G.J. Kovacs, G.D. Scott, Optical excitation of surface plasma waves in layered media, Physical Reviews B 16 (1977) 1297–1311.
[12] F. Yang, G.W. Bradberry, J.R. Sambles, Coupled surface plasmons at 3·391 μm, J. Mod. Opt. 37 (1990) 993–1003.
[13] Y. Wang, Wavelength selection with coupled surface plasmon waves, Appl. Phys. Lett. 82 (2003) 4385–4387.
[14] Guo, J., Tu, Y., Yang, L., Wang, L. & Wang, B. Design of a double grating-coupled surface plasmon color filter. In: *Optical Components and Materials XIII* vol. 9744 38–44 (SPIE, 2016).
[15] V. Narayanan, A. Arora, S.P. Amirtharaj, A. Krishnan, Plasmon-coupled hybrid Fabry–Pérot cavity modes in submicron metal–dielectric–metal arrays for enhanced color filtering, Opt. Eng. 58 (2019) 057109.
[16] B.-R. Huang, et al., Reduction of angular dip width of surface plasmon resonance sensor by coupling surface plasma waves on sensing surface and inside metal–dielectric–metal structure, J. Vac. Sci. Technol. A 31 (2013) 06F104.
[17] S. Mohapatra, R.S. Moirangthem, Theoretical study of modulated multi-layer SPR device for improved refractive index sensing, IOP Conf. Ser.: Mater. Sci. Eng. 310 (2018) 012017.
[18] P. Zhang, et al., A Waveguide-coupled surface plasmon resonance sensor using an Au-MgF2-Au structure, Plasmonics 14 (2019) 187–195.
[19] A.A. Alwahib, S.H. Al-Rekabi, W.H. Muttlak, Comprehensive study of generating sharp dip using numerical analysis in prism based surface plasmon resonance, AIP Conf. Proc. 2213 (2020) 020143.
[20] J. Feng, T. Okamoto, J. Simonen, S. Kawata, Color-tunable electroluminescence from white organic light-emitting devices through coupled surface plasmons, Appl. Phys. Lett. 90 (2007) 081106.
[21] K.T. Shimizu, R.A. Pala, J.D. Fabbri, M.L. Brongersma, N.A. Melosh, Probing molecular junctions using surface plasmon resonance spectroscopy, Nano Lett. 6 (2006) 2797–2803.
[22] H. Shin, S. Fan, All-angle negative refraction for surface plasmon waves using a metal-dielectric-metal structure, Phys. Rev. Lett. 96 (2006) 073907.
[23] M. Yoshida, S. Tomita, H. Yanagi, S. Hayashi, Resonant photon transport through metal-insulator-metal multilayers consisting of Ag and SiO_2, Phys. Rev. B 82 (2010) 045410.
[24] P.-T. Wu, M.-C. Wu, C.-M. Wu, A nanogap measuring method beyond optical diffraction limit, J. Appl. Phys. 102 (2007) 123111.
[25] P.-T. Wu, M.-C. Wu, C.-M. Wu, Measurement of the air gap width between double-deck metal layers based on surface plasmon resonance, J. Appl. Phys. 107 (2010) 083111.
[26] Y. Liu, J. Kim, Numerical investigation of finite thickness metal-insulator-metal structure for waveguide-based surface plasmon resonance biosensing, Sens. Actuators B 148 (2010) 23–28.
[27] Elements of the theory of interference and interferometers. in Principles of Optics: Electromagnetic Theory of Propagation, Interference and Diffraction of Light (eds. Wolf, E. & Born, M.) 286–411 (Cambridge University Press, Cambridge, 1999). doi: 10.1017/CBO9781139644181.016.
[28] I.R. Hooper, T.W. Preist, J.R. Sambles, Making tunnel barriers (Including Metals) transparent, Phys. Rev. Lett. 97 (2006) 053902.
[29] L. Xiang, et al., Strong enhancement of Goos–Hänchen shift through the resonant optical tunneling effect, Opt. Express, OE 30 (2022) 47338–47349.
[30] M.V. Davidovich, Resonant tunneling of photons in layered optical nanostructures (Metamaterials), Tech. Phys. 69 (2024) 1521–1530.

[31] M.-S. Tomaš, Recursion relations for generalized Fresnel coefficients: Casimir force in a planar cavity, Phys. Rev. A 81 (2010) 044104.
[32] A. Doval, C.D. Rodríguez-Fernández, H. González-Núñez, R. de la Fuente, Fresnel coefficients, coherent optical scattering, and planar waveguiding, Phys. Scr. 99 (2024) 026101.
[33] J.J. Monzón, L.L. Sánchez-Soto, E. Bernabeu, Influence of coating thickness on the performance of a Fabry–Perot interferometer, Appl. Opt., AO 30 (1991) 4126–4132.
[34] L.H. Smith, M.C. Taylor, I.R. Hooper, W.L. Barnes, Field profiles of coupled surface plasmon-polaritons, J. Mod. Opt. 55 (2008) 2929–2943.
[35] X. Wang, C. Yin, Z. Cao, Symmetrical Metal-Cladding Waveguide, in: X. Wang, C. Yin, Z. Cao (Eds.), Progress in Planar Optical Waveguides, Springer, Berlin, Heidelberg, 2016, pp. 145–162, https://doi.org/10.1007/978-3-662-48984-0_6.
[36] C. Filgueira-Rama, A. Doval, Y. Arosa, R. de la Fuente, Beneath and beyond frustrated total reflection: a practical demonstration, Am. J. Phys 93 (2025) 157–163.
[37] M.A. Ordal, R.J. Bell, R.W. Alexander, L.L. Long, M.R. Querry, Optical properties of fourteen metals in the infrared and far infrared: Al, Co, Cu, Au, Fe, Pb, Mo, Ni, Pd, Pt, Ag, Ti, V, and, Appl. Opt., AO 24 (1985) 4493–4499.
[38] J. Gong, R. Dai, Z. Wang, Z. Zhang, Thickness dispersion of surface plasmon of Ag nano-thin films: determination by ellipsometry iterated with transmittance method, Sci. Rep. 5 (2015) 9279.
[39] A. Ciesielski, L. Skowronski, M. Trzcinski, T. Szoplik, Controlling the optical parameters of self-assembled silver films with wetting layers and annealing, Appl. Surf. Sci. 421 (2017) 349–356.
[40] M. Ferrera, M. Magnozzi, F. Bisio, M. Canepa, Temperature-dependent permittivity of silver and implications for thermoplasmonics, Phys. Rev. Mater. 3 (2019) 105201.